Dynamic Behavior of the Flow Field in a RIM Machine Mixing Chamber

Ricardo J. Santos, Ertugrul Erkoç, and Madalena M. Dias
Laboratory of Separation and Reaction Engineering, Chemical Engineering Dept., Faculdade de Engenharia da Universidade do Porto, Portugal

José Carlos B. Lopes
Laboratory of Separation and Reaction Engineering, Chemical Engineering Dept., Faculdade de Engenharia da Universidade do Porto, Portugal

Fluidinova, Engenharia de Fluidos, S.A., Maia, Portugal

DOI 10.1002/aic.11771
Published online May 5, 2009 in Wiley InterScience (www.interscience.wiley.com).

Dynamic behavior of the flow field in a Reaction Injection Molding, RIM, machine mixing chamber, having dimensions typically used in industrial machines, is studied from dynamic velocity data of Laser Doppler Anemometry, LDA, measurements and Computational Fluid Dynamics, CFD, simulations with a 2D model. This study is based on the spectral analysis of the dynamic flow field data. The typical frequencies, in the reactor flow field, are identified and its values are related to the identified flow structures. The differences between the typical frequencies from experiments and simulations are observed and justified on the basis of the 2D representation of a 3D cylindrical geometry. © 2009 American Institute of Chemical Engineers *AIChE J,* 55: 1338–1351, 2009
Keywords: mixing, fluid mechanics, computational fluid dynamics (CFD), polymer processing

Introduction

In high pressure Reaction Injection Molding, RIM, machines the heart of the process is the impinging of two high-speed jets, up to 100 m/s, in a confined cylindrical mixing chamber. The geometry of the mixing chamber studied in this work has dimensions of a typical industrial high pressure RIM machine, with a chamber diameter of 10 mm[1] and jets diameter of 1.5 mm, as shown in Figure 1. The Reynolds number for this process was originally defined at the injectors as[2]

$$Re = \frac{\rho v_{\text{inj}} d}{\mu} \tag{1}$$

where v_{inj} is the superficial velocity at the injectors, d the injectors diameter, ρ the fluid density and μ the fluid viscosity. The monomer fluids generally used in RIM have viscosities up to 1 Pa·s and thus, although the high speed of the jets, the typical Reynolds numbers for this process are low, in the range of 100–600.[3]

Previous Laser Doppler Anemometry, LDA, measurements[4,5] in the RIM machine mixing chamber, have clearly shown that the jets impingement point oscillates. The oscillatory behavior occurs above a transition *critical Reynolds number*, which was observed in the literature to have its onset at $Re \approx 90$,[6] although fully developed oscillations were only reported at $Re = 120$.[7,8] Further characterization of the flow field was made with Particle Image Velocimetry, PIV,[7] and from the PIV results it was observed that:

- Below the critical Reynolds number, the flow field presents a very weak dynamic with low amplitude flow oscillations from $Re = 100$ to 120,[6,9] which are not strong enough to break a noticeably observable flow field symmetry plane located between the two directly opposite injectors.
- Above the critical Reynolds number, the flow field regime is chaotic. Downstream of the jets impingement point

Correspondence concerning this article should be addressed to J. C. B. Lopes at lopes@fe.up.pt

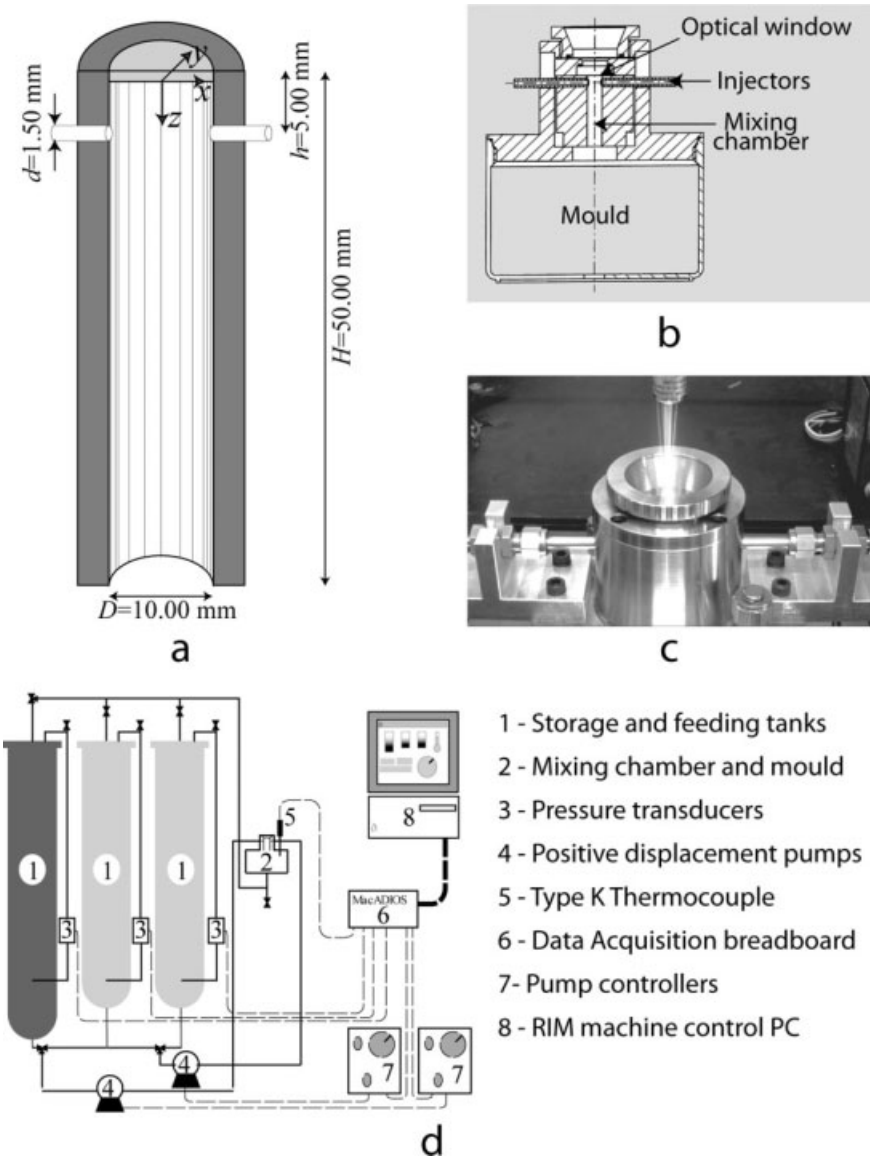

Figure 1. Pilot RIM machine: (a) mixing chamber geometry and dimensions; (b) sketch and drawing of mixing chamber with mould; (c) photography of mixing chamber; (d) flow chart and instrumentation.

circular vortices are formed and detached towards the outlet forming a vortex street throughout the chamber. This vortices are the main mixing mechanism in RIM and are always associated with strong jets oscillations.[10]

Published literature on opposite impinging jets dynamics[11,12] and in particular confined impinging jets at laminar regime[5,6,9,13–15] is scarce. The few works characterizing the oscillation frequencies of the jets were mostly done for $Re < 200$,[6,9] and studies for higher values of Re come from the research team of this article.[5,13,16] The absence of studies in the industrial range of operation Reynolds numbers could be due to difficulties such as those reported by Johnson and Wood[9] in measuring frequencies for $Re > 150$. In this study the Reynolds numbers will be at least twice the value of the Re marking the onset of jets oscillations, covering for the first time the range of values of industrial interest not found in the literature, $250 \leq Re \leq 600$.

In this work it is depicted for the first time the underlying mechanisms determining the jets oscillations frequencies from the analysis of the flow structures geometry. The flow oscillation mechanisms was only once studied[13] from spring theory. This is a new result and was only possible due to dynamic flow field simulation, which established the relation between the jets dynamic behavior and the flow field structures. The study of the jets oscillations dynamics in RIM is of extreme industrial relevance since the oscillations are always connected to the main mixing mechanisms in RIM[8]: the vortex street. On the other hand mixing determines the polymer properties in RIM.[17,18]

Data Analysis Procedure

The time series obtained from both simulations and experiments were transformed into the frequency domain, f,

using the Fast Fourier Transform and the slotted correlation method.[19,20] The procedures for the time series transformation in frequency power spectra are reported in the Appendix.

The frequency values presenting higher energies in the power spectra are here referred as *typical frequencies*, ϕ, and they are the more representative values of the frequency of the oscillatory phenomenon. For a direct comparison between the values of ϕ, the Strouhal number defined as

$$St = \frac{\phi d}{\upsilon_{\text{inj}}} \tag{2}$$

was computed. The Strouhal number allows checking if changes of ϕ with *Re* are only due to the increase of υ_{inj}.

Experiments

Experimental setup

For this study a pilot RIM machine was built. A flowchart with the instrumentation is shown in Figure 1 along with some views of the experimental set-up. A detailed description of the RIM machine is presented in Teixeira et al.[5]

The object of this study is the flow field in the cylindrical mixing chamber, having dimensions typical of industrial RIM machines: diameter $D = 10.00 \pm 0.05$ mm, and height $H = 50.00 \pm 0.05$ mm. The injectors are 50 mm long in order to ensure a fully developed Poiseuille flow of the jets at the chamber entrance and consist of a tube with a measured diameter $d = 1.496 \pm 0.001$ mm. The injectors centre is located at 5.0 mm from the top of the mixing chamber. In order to allow the penetration of the laser beams for LDA measurements, the top of the chamber consists of an optical window made from synthetic fused silica. The mixing chamber discharges the fluid to a cylindrical mould that has 15.0 cm diameter and 10.0 cm height. Figure 1 shows a sketch and a photograph of the mixing chamber with the mould and injectors.

For the LDA measurements the 2D backscattering system from TSI® was used, but having a larger probe than in Teixeira et al.[5] The main difference caused by the new probe usage is the LDA measuring volume dimensions that became 3.169 mm in length and 0.153 mm in diameter. The length of the LDA volume is always aligned in the z direction as shown in Figure 1. Only the x velocity component, see Figure 1, is measured with LDA at various positions ($z = 5.0$, 7.5, 10.0, and 12.5 mm) along the mixing chamber axis. Figure 1a also shows the positioning of the coordinates axis origin in the mixing chamber.

Experimental conditions and accuracy

The liquid used in the experiments is an aqueous solution with a glycerine mass fraction, $X_{\text{glycerine}}$, of 72.2%. The density and the viscosity were determined as functions of temperature. The density is determined by

$$\rho = \left(1 - X_{\text{glycerine}}\right)\rho_{\text{water}} + X_{\text{glycerine}}\rho_{\text{glycerine}} \tag{3}$$

where $\rho_{\text{water}}(\text{kg/m}^3)$ and $\rho_{\text{qlycerine}}(\text{kg/m}^3)$ are the water and glycerine densities respectively, which are functions of the temperature, θ(K), $\rho_{\text{water}} = 1064.60 - 0.23\theta$, and $\rho_{\text{qlycerine}} = 1440.50 - 0.61\theta$.

For the viscosity, the experimental data obtained with a PaarPhysica UDS 200 rheometer in the ranges $20^\circ\text{C} \le \theta \le 30^\circ\text{C}$ and $0 \le X_{\text{glycerine}} \le 88\%$ was well fitted by

$$\mu = \left(\left(1 - X_{\text{glycerine}}\right)\left(A_{\text{water}} e^{\frac{B_{\text{water}}}{\theta}}\right)^a + X_{\text{glycerine}}\left(A_{\text{glycerine}} e^{\frac{B_{\text{glycerine}}}{\theta}}\right)^a \right)^{1/a} \tag{4}$$

where μ is the viscosity in mPa·s, and the constants are given by: $A_{\text{water}} = 5.17 \times 10^{-4}$ mPa · s, $B_{\text{water}} = 2.22 \times 10^3$ K, $A_{\text{glycerine}} = 7.06 \times 10^{-9}$ mPa · s, $B_{\text{glycerine}} = 7.64 \times 10^3$ K, $a = -0.320$.

The viscosity and density curves as functions of temperature were used to set the *Re* for each experiment. Thus, for each value of *Re*, the jets average velocity, υ_{inj}, and the Froude number, *Fr*, are functions of the temperature. The Froude number is defined as

$$Fr = \frac{\upsilon_{\text{inj}}^2}{dg} \tag{5}$$

where d is the injectors' diameter and g is the gravity acceleration. During each measurement, the temperature was considered constant, since each data series was acquired in a short period, approximately 1 min. The total number of points in each series is 10^5. Detailed description of the LDA experiments throughout the mixing chamber axis is given in Santos.[7]

The maximum measured experimental error associated to the Reynolds number is 10%.[7] The error was determined from setting the Reynolds number in the pilot RIM control graphic interface and then measuring the actual Reynolds number from the flow rate and fluid temperature.

LDA parameters

LDA measurements were made in time stamp mode, i.e., when a velocity datum is computed and recorded the time information is also recorded, with a precision of up to 10^{-6}s. A single velocity component, υ_x, was measured using the laser beams with the wavelength of 514.5 nm.

The Doppler signal has a frequency that is determined by the particle velocity and fringe spacing. The half angle of intersection of the laser beams is 2.76° and the fringe spacing is 5.35 μm. Considering a value of υ_{inj} equal to twice the one for the most extreme case of $Re = 600$, the LDA signal frequency would be 314 kHz. The frequency shift chosen was 2000 kHz, which resolves any directional ambiguity under these conditions. The band pass filter for LDA backscattering signal was set in the range of 300–3000 kHz, preventing the elimination of any of the velocity values in the expected range for this application that are comprised in the interval between 2000 − 314 and 2000 + 314 kHz.

Data analysis procedure–LDA

Table 1 lists the slotted correlation parameters used for the experimental LDA time series analysis. The choice of different parameters was based in the acquisition data rates,

Table 1. Slotted Correlation Parameters for the Different Measuring Points

Measuring Point	t_s[ms]	Δt[ms]
$z = 0.5$ mm	5.00×10^{-1}	2.50×10^{-1}
$z = 7.5$ mm	5.00×10^{-1}	2.50×10^{-1}
$z = 10.0$ mm	1.00	5.00×10^{-1}
$z = 12.5$ mm	1.00	5.00×10^{-1}

f_s, that are higher at $z = 5.0$ and $z = 7.5$ mm. The value of the slot width (see the Appendix), Δt, was set to half of slotted correlation time interval, t_s, which gives a probability of 1/2 of finding at least one value in each slot. Other values for these parameters were tested in a systematic way. It was clear, from the resulting frequency power spectra, that there is a range of values of t_s and Δt over which the spectra are not significantly altered, yet for values out of that range, phenomena such as the smoothing of the energy peaks in the power spectrum are observed.

The power spectra from the LDA time series with 10^5 points are too complex to extract useful information, as can be seen from Figure 2 where the power spectra from the time series took at $z = 5.0$ mm are shown. To get further insight from the frequency power spectra, the full time series was divided into 25 sub-series of 4000 points each. Particular power spectra from the sub-series taken at $z = 5.0$ mm are shown in Figure 3. Although dividing the time series disperses the information by various power spectra, the fact that these power spectra present well defined frequency peaks allows an immediate identification of the *typical frequency of oscillation*, ϕ.

Results presentation

Figure 2 shows the plots of the normalized power spectra obtained at $z = 5.0$ mm from the time series of v_x with 10^5 samples. For each Reynolds number only a representative plot, out of the six experiments made, is shown in Figure 2. The complexity of the oscillatory behavior, in this range of Reynolds numbers, is clearly seen from Figure 2, where all the power spectra present a generally large spread of energy around some typical frequency values. This spread of energy shows that the system is not oscillating with a single frequency but rather within a range of typical frequencies, which makes the interpretation of power spectra from long time series a difficult task.[9] The complexity of the power spectra can be a proof of chaos, since the spreading of energy around the typical frequency of a phenomenon is one of the signatures of chaotic systems; or it can be due to the different flow structures captured by the LDA measuring volume.[5]

From the power spectra in Figure 2, it is also observed that the energy peaks are better defined at lower Reynolds numbers, $Re = 250$. For higher values of Re there is the appearance of some low frequency phenomenon that is probably associated to changes in the value of the jets oscillation frequency and to transient periods where the jets are probably not oscillating. This low frequency can also be triggered by other mechanisms. A good candidate is the increasing interaction, observed from flow imaging,[21] between the jets and the flow field structures around the jets that are two pairs of vortices formed up and down the jets. These flow structures, specially the vortices that are behind the jets impingement point, present increasing distortion and time evolution at higher values of Re and may influence the jets

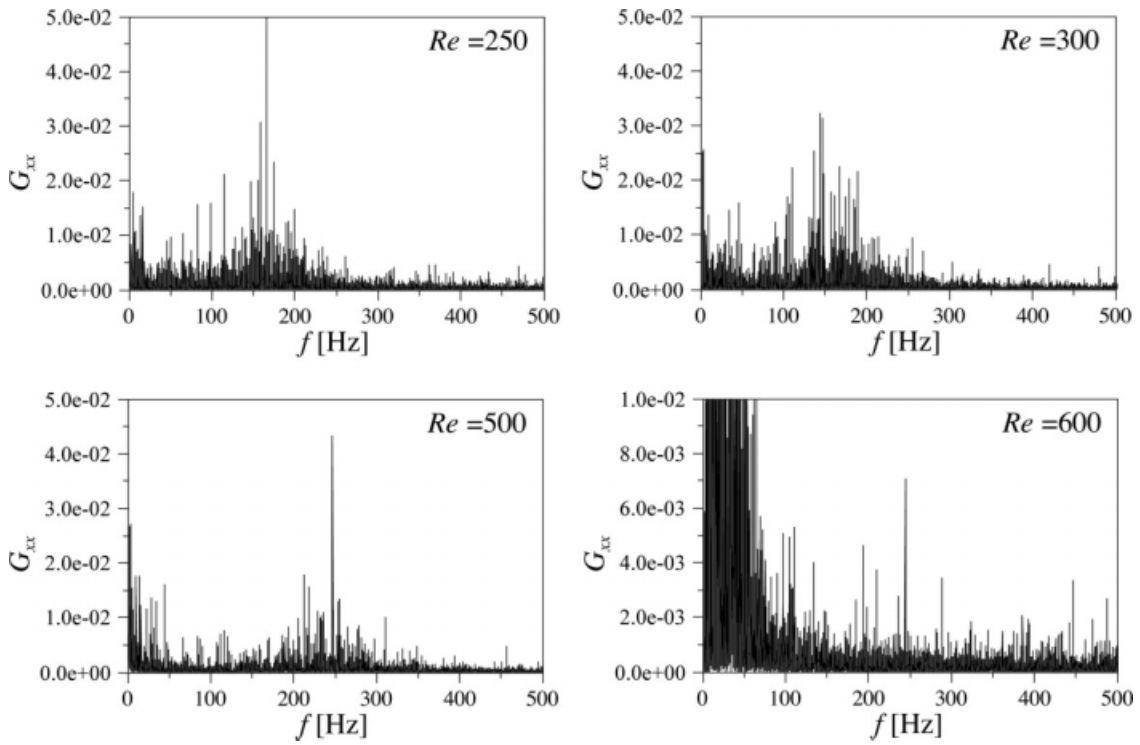

Figure 2. Normalized power spectra of the measured velocity component v_x for $z = 5.0$ mm and $Re = 250$, 300, 500 and 600. Complete time series.

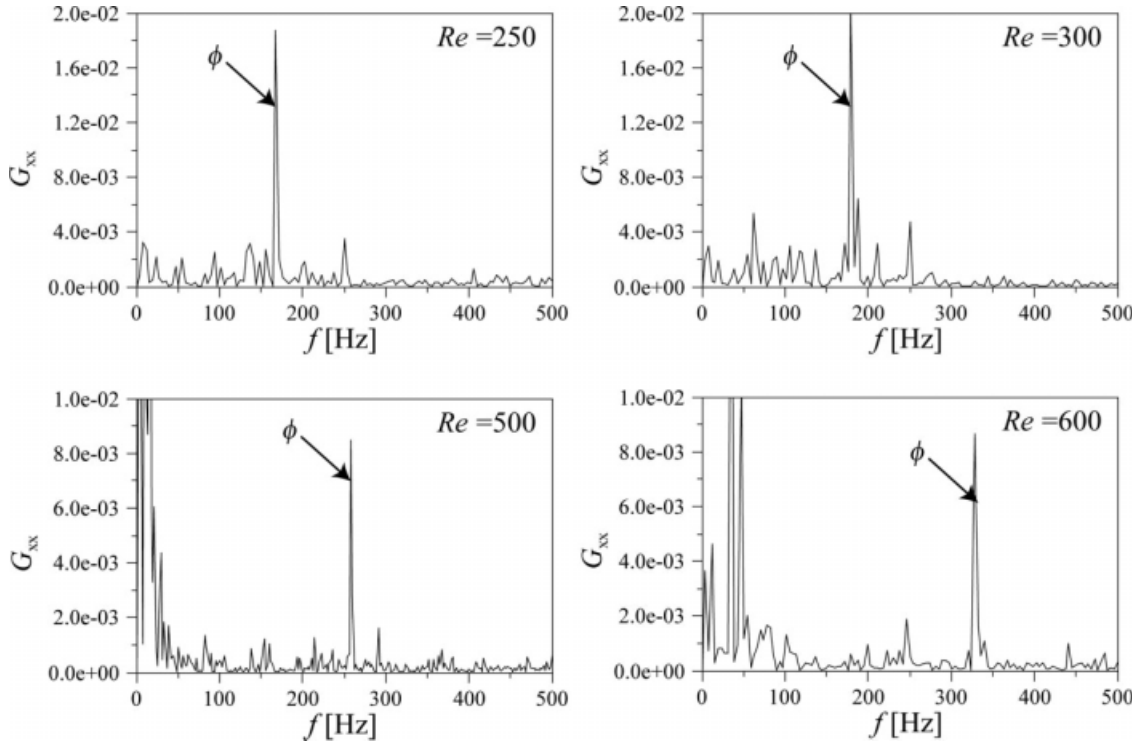

Figure 3. Normalized power spectra of the measured velocity component v_x for z = 5.0 mm and Re = 250, 300, 500 and 600. Sub-series of 4000 points.

dynamics. An exception to this trend is experiment 6 at $Re = 500$, shown in Figure 2, where the frequency of jets oscillation presents a well defined value, i.e., with very little energy spreading around the energy peak. This indicates the possibility of the system to have oscillations within a narrow range of frequencies over long periods, even at the higher Reynolds numbers used in the industrial RIM processes.

For each Reynolds number the typical frequencies, ϕ, were identified from the power spectra of each sub-series, of which representative power spectra are shown in Figure 3. The power spectra of the sub-series have clear energy peaks, allowing an easy identification of the typical frequencies. From the several values of ϕ, for each value of Re, the average and standard deviation for St were obtained and are shown in Figure 4. The bars in Figure 4 represent the standard deviation around the average value of St for each Re. These bars serve the purpose of illustrating the dispersion of oscillatory states, i.e., oscillation frequencies, in which the system may be found.

As it can be seen from Figure 4, for all values of z that the Strouhal number is kept almost constant and inside the variance limits given by the bars. Nevertheless, it is clear a slight decreasing trend of St towards higher values of Re. The invariability of St with Re shows that the typical frequency values directly scale with v_{inj}. The average value of St decreases slightly as z increases, from $St = 0.062$ for $z = 5.0$ mm to $St = 0.045$ for $z = 12.5$ mm.

Results interpretation

The results are interpreted from the hypothesis that the typical frequencies of the jets impingement point oscillation are associated to the formation of vortices. Here, such as in Vortex Induced Vibrations where it is considered that a bluff body is in resonance when its vibration frequency is the same with the natural vortex shed frequency,[22] it is proposed that the jets impingement point is vibrating at the same frequency of the vortices formation rate.

To check this hypothesis the shape of the vortex was imaged from a dynamic CFD simulation of the 3D flow field made in Fluent™ at $Re = 200$. The shape of the vortices can be seen from the several vector maps of the same time instant shown in Figure 5. The vortices are elongated ellipsoids, prolate spheroid, having a polar diameter d_2, between 3 and 6 mm, and an equatorial diameter $d_1 = 3$ mm. The polar diameter is inferred from the disappearance of the vortices centers at $y = 3$ mm.

The simulated 3D flow field is consistent with the experimental flow field visualization made at the 2D xz plane $y = 0$, i.e., containing the injectors and mixing chamber axis. The experimental visualization consisted of the 2D vector maps[7] obtained with 2D Particle Image Velocimetry, PIV, and tracer maps obtained with Planar Laser Induced Fluorescence, PLIF, which are shown in Figure 6. The experiments confirmed the flow structures imaged from the CFD simulations, i.e., at the jets impingement region there is the formation of a pancake like structure[6] and immediately downstream the jets there is the formation of two circular vortices.

The typical frequency of the jets oscillation is predicted assuming that each oscillation of the jets impingement point is produced from the formation of a pair of vortices. The PLIF results in Figure 6 show that the jets are "feeding" the vortices with fluid. If each vortex is "filled" and then detached, its formation rate is the ratio of the injector flow

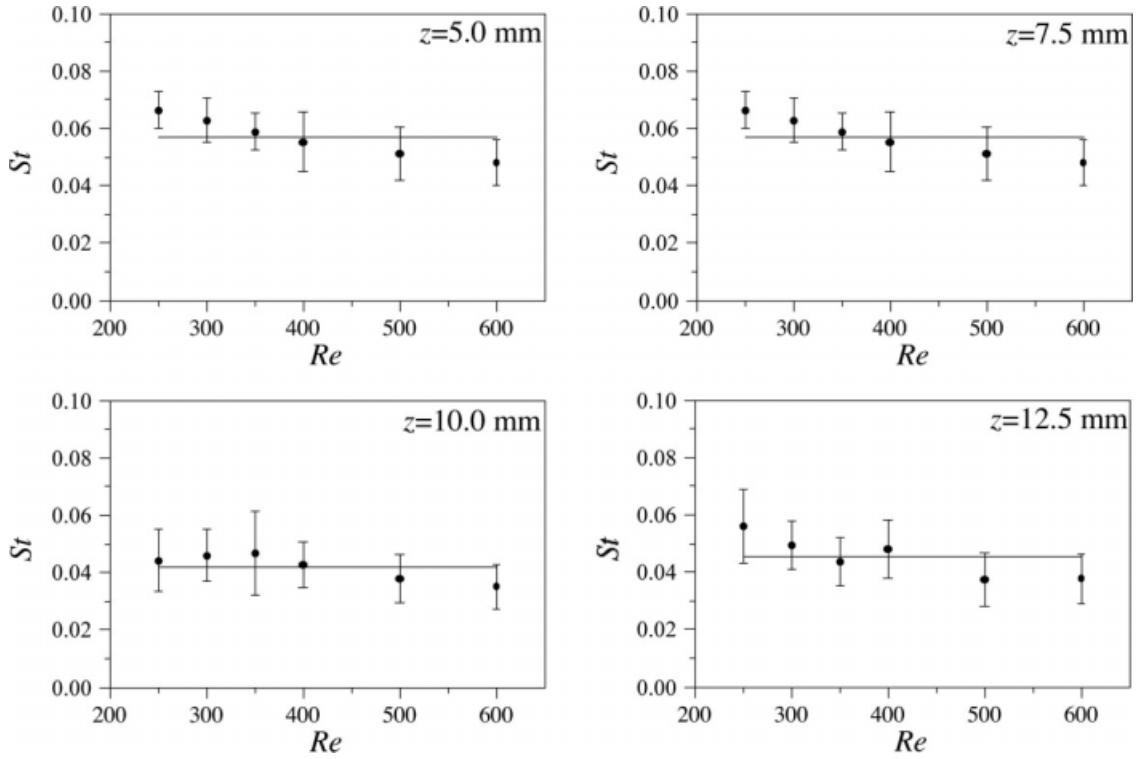

Figure 4. Evolution of the experimental Strouhal number with the Reynolds number at z = 5.0, 7.5, 10.0 mm and 12.5 mm.

rate, q_{inj}, to the vortex volume, V_{vortex}, i.e., q_{inj}/V_{vortex}. Each pair of formed vortices displaces the impingement point to one side and the next pair to the opposite side. A complete oscillation of the jets impingement point only occurs when two pairs of vortices are formed, and so the vortices formation frequency is

$$\phi_{vortex} = \frac{1}{2}\frac{q_{inj}}{V_{vortex}} \tag{6}$$

The vortices are ellipsoids with volume

$$V_{vortex} = \frac{\pi d_2 d_1^2}{6} \tag{7}$$

For a Strouhal number close to $St = 6 \times 10^{-2}$ the vortex polar diameter, d_2, computed from Eqs. 2, 6, and 7 is around 5 mm. As seen in Figure 5 the right hand side vortex below the jets, which is clearly seen at the xz planes at $y = 0$ and $y = 1.5$ mm, vanishes in the xz plane at $y = 3$ mm, a consistent observation with the suggested value for d_2. Increasing the Reynolds number the St decreases, as shown in Figure 4, thus indicating a growth of d_2, since as observed from PIV results,[21] the equatorial diameter is roughly constant with the Re.

Simulations

Model

To confirm the hypothesis that the jets impingement point vibrations are determined by the vortices formation dynamic, CFD simulations were performed. A simplified 2D model of the mixing chamber, using less computational resources than a 3D geometry, was used in order to obtain lengthy time series and sweeping of several Re. The 2D model used for the flow field simulation was described in detail by Teixeira.[4] The model consists of an axial cut of the mixing chamber passing through the injectors centre, the xz plane at $y = 0$ in Figure 5. In Figure 7 the model geometry is shown and the boundary conditions summarized. The dimensions of the 2D model are those of the 3D geometry of the experimental mixing chamber, and the Reynolds number defined in the same way. Extensive numerical and experimental validation of the 2D model simulation results are presented in Teixeira[4] and Santos.[7]

Data analysis procedure–CFD

For immediate comparison between the power spectra from different Re the data is presented in a dimensionless form, where the dimensionless frequency is computed as

$$f' = \frac{f\,d}{v_{inj}} \tag{8}$$

For the CFD simulation, the data rates are the same regardless of the spatial location of the probed point, and so the values for the parameters t_s and Δt are constant. These parameters are set to values equivalent to the ones used for the LDA measurements, $t_s = 0.500$ ms and $\Delta t = t_s/2$.

The system evolution is clear from the dynamic sequence of vorticity and streamline maps, presented in Figure 8, and from the time history of x velocity component at the jets impingement point for $Re \geq 250$, presented in Figure 9. In

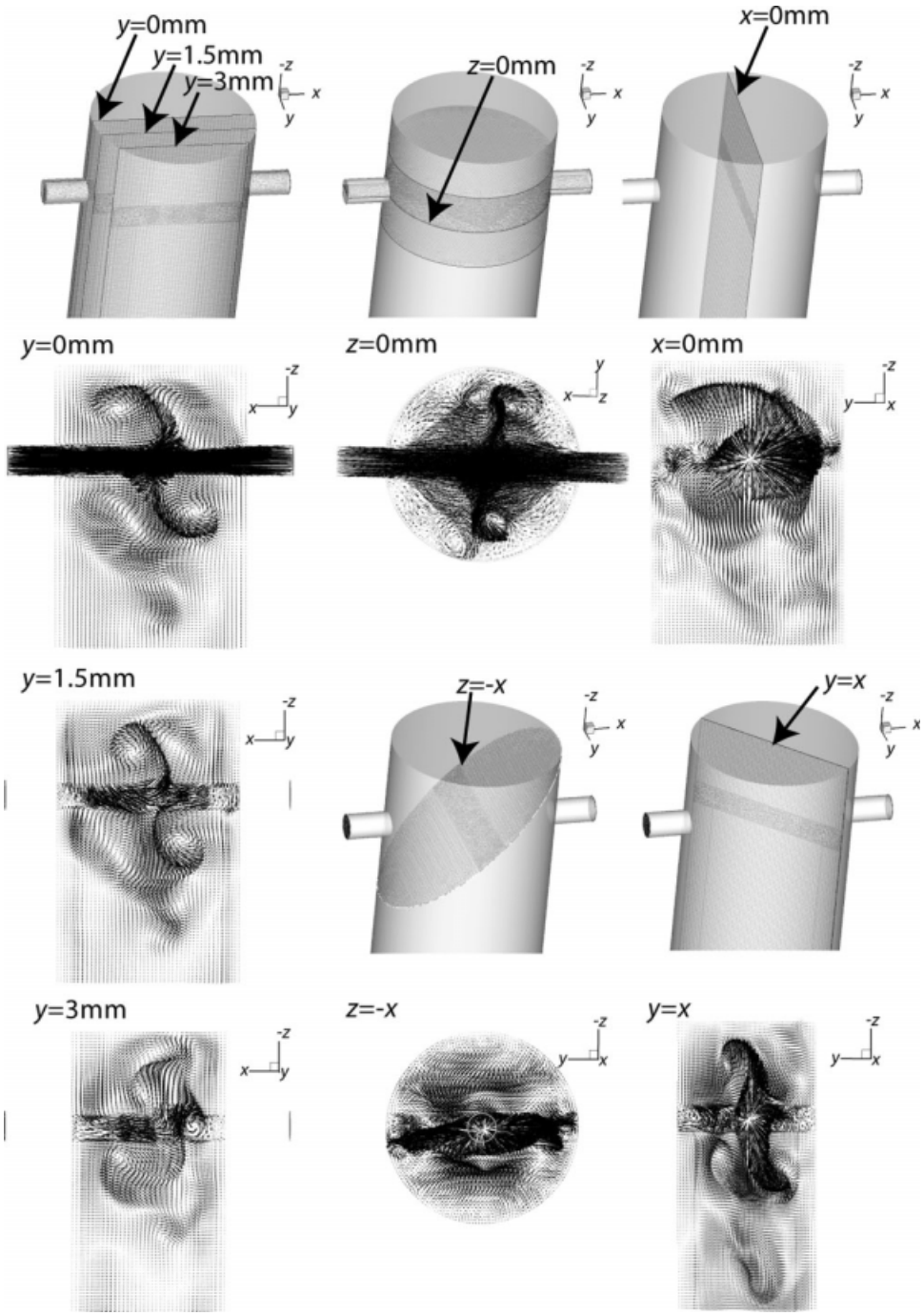

Figure 5. Flow imaging: vector maps from dynamic 3D CFD simulation at *Re* = 200.

both figures time is defined in terms of t/τ, where τ is the passage time in the mixing chamber. For the CFD simulations results the velocity is rendered dimensionless with the average superficial velocity at the injectors, i.e., $v_x^* = v_x/v_{inj}$.

The vorticity and streamline maps in Figure 8 show an initial steady state for both $Re = 300$ and $Re = 500$, which presents complete segregation between both sides of the mixing chamber. This is clear from the streamlines that show the jets' path from the injectors to the outlet. The opposite jets impinge in the chamber axis and bend towards the outlet flowing side by side without mixing throughout the chamber axis. On dynamic chaotic states, after the jets impingement point, a sequence of counter rotating vortices appears, as can be seen from the positive and negative values of vorticity in Figure 8, i.e., a vortex street is formed. The jets circulate around these vortices as can be seen from the streamlines. Mass transfer simulations showed that in chaotic states the fluid streams from both injectors are engulfed in the vortex street promoting a very fast homogenization.[10]

From the time histories of v_x^*, shown in Figure 9, a *warm-up time* of about 1.8 τ is observed, which is the time the

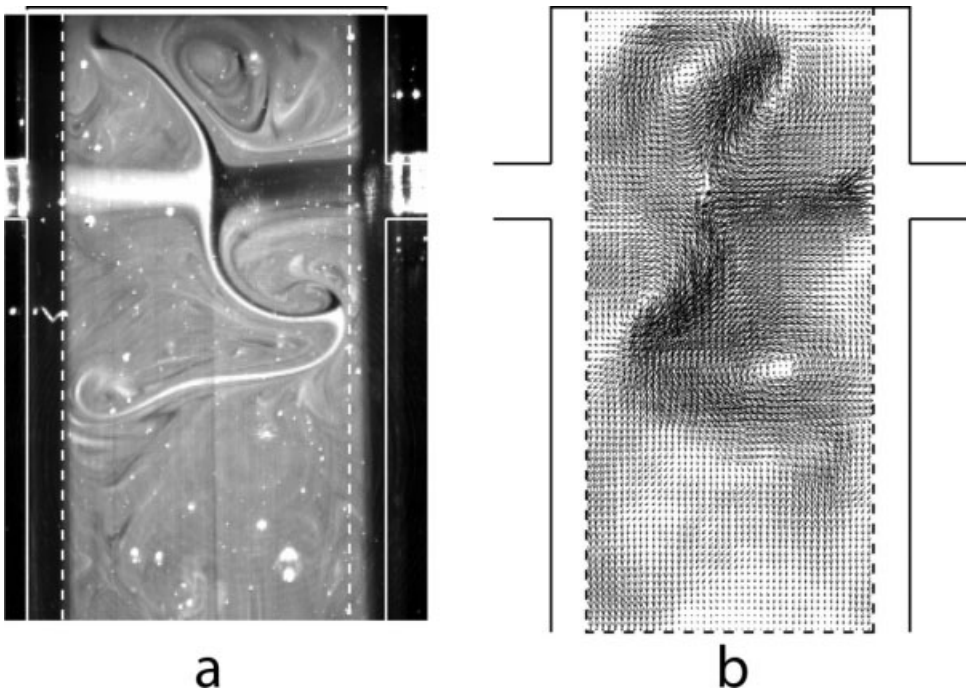

Figure 6. Images of the flow field at *Re* = 200 in the *xz* plane containing the chamber and injectors axis, *y* = 0, using: (a) Planar Induced Fluorescence, and (b) 2D Particle Image Velocimetry.

system takes to evolve from the initial steady state to fully developed chaotic states with jets oscillations. Although it takes only 1.8 τ for the onset of the fully developed oscillations, in this work the first 2.5 τ of the time series were not used for the spectral analysis.

For a better comparison between the spectral analysis of CFD results and the LDA data, the CFD time series were modified. The dynamic flow field simulations were done up to 10 τ, and since the first 2.5 τ were removed, the analyzed time series had a total time of 7.5 τ, which is about 200 times shorter than the experimental data. The number of points per 7.5 τ is about 2×10^4 that is, with data rates of the order of 7×10^4 Hz, about 20 times higher than the LDA measurements at the impingement point. The time series was repeated 200 times and sampled at every 20th to 30th point in order to keep its data rates between 2800 and 3500 Hz, which is close to LDA data rates at the impingement point.

The power spectra for the CFD results presented clear energy peaks at the values of the typical frequencies and thus, contrary to the LDA data, no further treatment of the time series was done.

Results

The power spectra for $Re = 250$, 300, 400, and 500 of the time series of v_x^* at the jets impingement point, $x = 0$ and $z = 5.0$ mm, are shown in Figure 10. From the power spectra at $z = 5.0$ mm a very clear oscillatory behavior of the jets with a well defined frequency is observed. The average value of the *St* at the impingement point is 0.099 ($\approx$ 0.10), from the four simulated *Re*. For high values of *Re* the typical frequency energy peak loses its definition and the energy becomes more spread around $St = 0.10$. From the time history at $Re = 500$ the appearance of a second oscillatory behavior at the impingement point with a lower frequency is observed. This lower frequency oscillation is probably induced by the fully developed vortices formed downstream in the mixing chamber that are increasingly affecting the jets oscillations for higher Reynolds numbers.

The loss of definition in the energy peak at higher Reynolds numbers is also due to the increasing interaction of the jets with the surrounding fluid as can be seen in Figure 8.

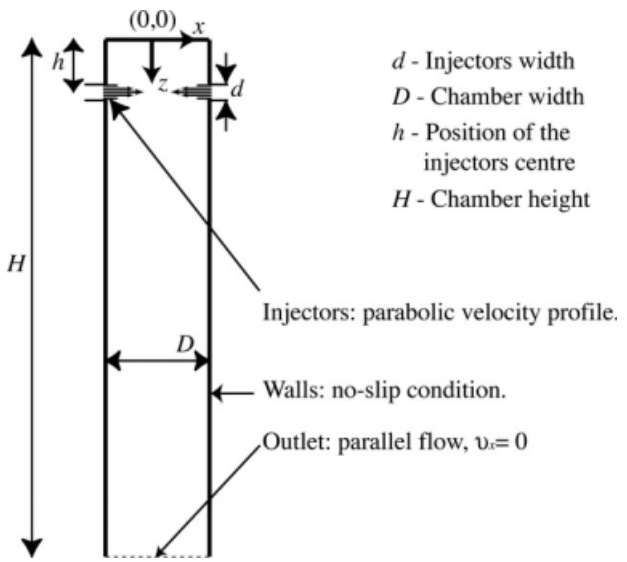

Figure 7. Geometric model used in the CFD simulations and boundary conditions.

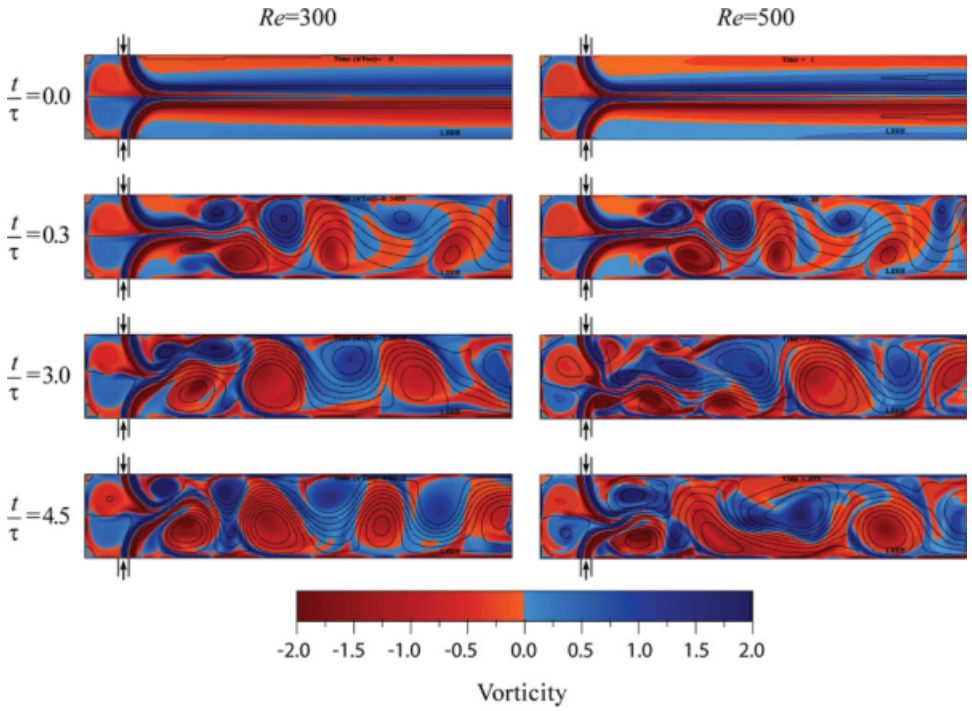

Figure 8. Vorticity and streamline maps from the *Re* = 300 and *Re* = 500 simulations.

[Color figure can be viewed in the online issue, which is available at www.interscience.wiley.com.]

For $Re = 500$ the jets are more disturbed in their path than for $Re = 300$ and hence their oscillation frequency becomes more random. Thus increasing the Reynolds number increases the interaction between several flow structures inside the mixing chamber. This low frequency phenomenon affecting the impingement point oscillation was also observed in the experimental data.

The power spectra at other locations in the mixing chamber, $z = 2.0$, 5.0, 11.0, 22.0, and 33.0 mm, are shown in Figure 11 for $Re = 300$. At other Reynolds numbers the power spectra are similar, and thus only the illustrative case of $Re = 300$ is shown.

The oscillations frequency at $z = 2.0$ mm is mainly controlled by the jets as can be seen from the frequency power spectra of v_x^* shown in Figure 11. The value of the Strouhal number, St, is kept around 0.1, which is the typical St at the jets impingement point as also seen from Figure 10. Some additional low frequency phenomenon influences the v_x^* history at $z = 2.0$ mm. For $Re = 300$ the low frequency phenomenon generates a single energy peak coincident with the values of the peaks observed for $z \geq 11.0$ mm, and thus its presence is probably associated to the formation of the *fully developed vortices* downstream the chamber.

From the v_x^* time histories at $z = 2.0$ mm it is seen that the amplitude of the movement of the vortices that are behind the jets impingement point increases with Re due to a growing influence of the jets oscillation to upstream positions in the mixing chamber. The greater influence of the jets on the vortices that are behind the jets impingement at higher values of Re is also seen in the vorticity maps in Figure 8, where it is clear that the shape of the vortices is more distorted for $Re = 500$ than for $Re = 300$ due to the jets influence.

The vortices structures are formed in pairs, and each pair of detached vortices generates half an oscillation of the jets impingement point, which could be seen from the dynamic visualization of the CFD results. The oscillation frequency is given by

$$\phi_{\text{vortex}} = \frac{q_{\text{inj}}}{2V_{\text{vortex}}} = \frac{dv_{\text{inj}}}{2A_{\text{vortex}}} \tag{9}$$

where q_{inj} is the flow rate of each injector, V_{vortex} is the volume of each vortex and A_{vortex} its area. The vortices have circular shape and using the wave frequency dimensionless value, St, the vortex diameter, D_{vortex2D}, is determined by:

$$D_{\text{vortex2D}} = \sqrt{\frac{4d^2}{2\pi St}} \tag{10}$$

From the average Strouhal number, $St = 0.10$, the formed structures are discs with a diameter of approximately 3.8 mm. If these discs are formed simultaneously there is a free space of approximately 2 mm that is occupied by the jets, as can be observed in Figure 8.

For positions away from the injectors, as in the case of the time histories at $z = 11.0$ mm, Figure 9, it can be seen that the flow oscillation amplitude is now larger than at $z = 5.0$ mm, due to the fact that the flow is no longer trapped between two well balanced opposite forces, the jets, that constrain its capability to oscillate.

At $z = 11.0$ mm the St value is kept around 0.1, see Figure 11, and thus the influence of the same flow structure that

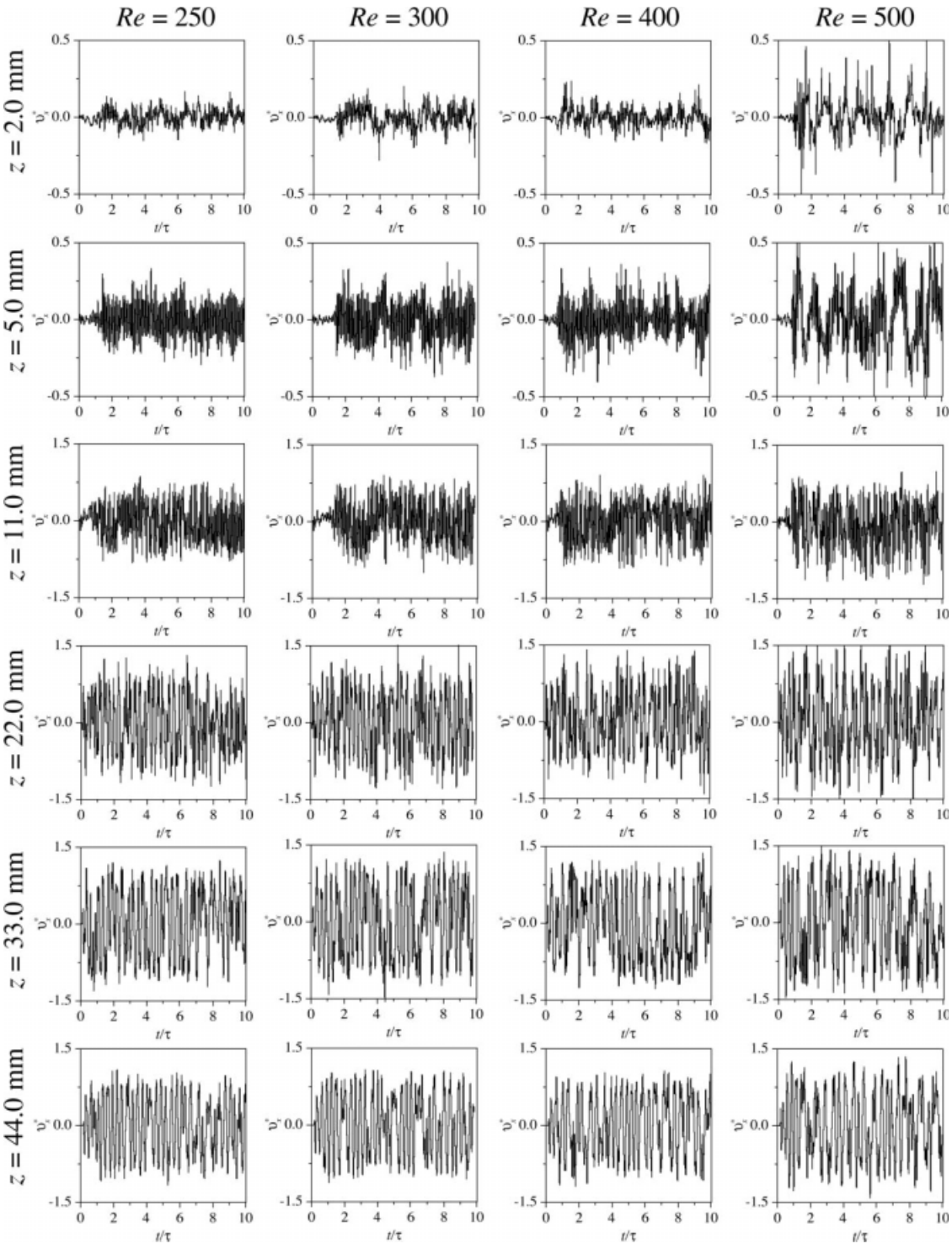

Figure 9. Time histories of v_x^* throughout the mixing chamber axis in the range of 250 ≤ *Re* ≤ 500.

dictates the value of $St \approx 0.1$ at $z = 5.0$ mm still prevails. For $z \geq 22.0$ mm, as it can be seen from the v_x^* time histories and power spectra, the flow characteristics are constant throughout the chamber with $St \approx 0.03$ and larger flow oscillation amplitudes. This typical frequency value, $St \approx 0.03$, is generated by the passage of fully developed vortices extending throughout the whole chamber width but keeping their diameter while evolving through the mixing chamber, as seen from Figure 8. Each pair of counter rotating fully developed vortices, formed with fluid from both jets, generates a single wavelength while passing through a fixed point, which yields an oscillation frequency,

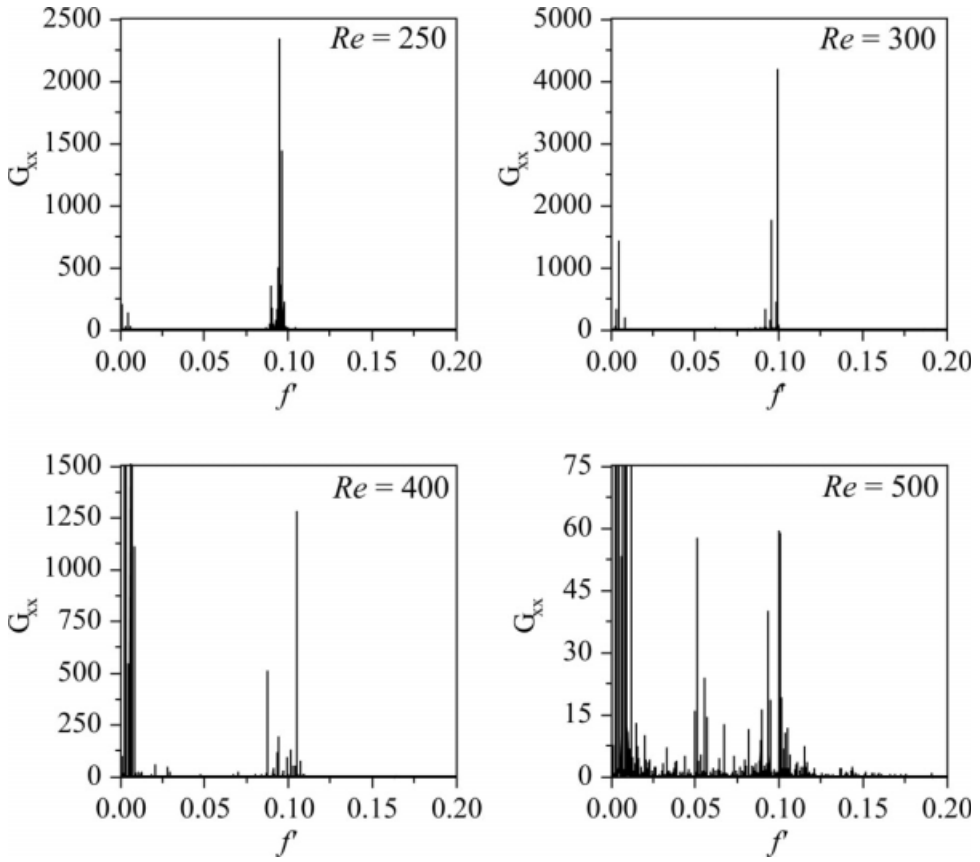

Figure 10. Power frequency spectra of v_x at the impingement point in the range of 250 ≤ *Re* ≤ 500.

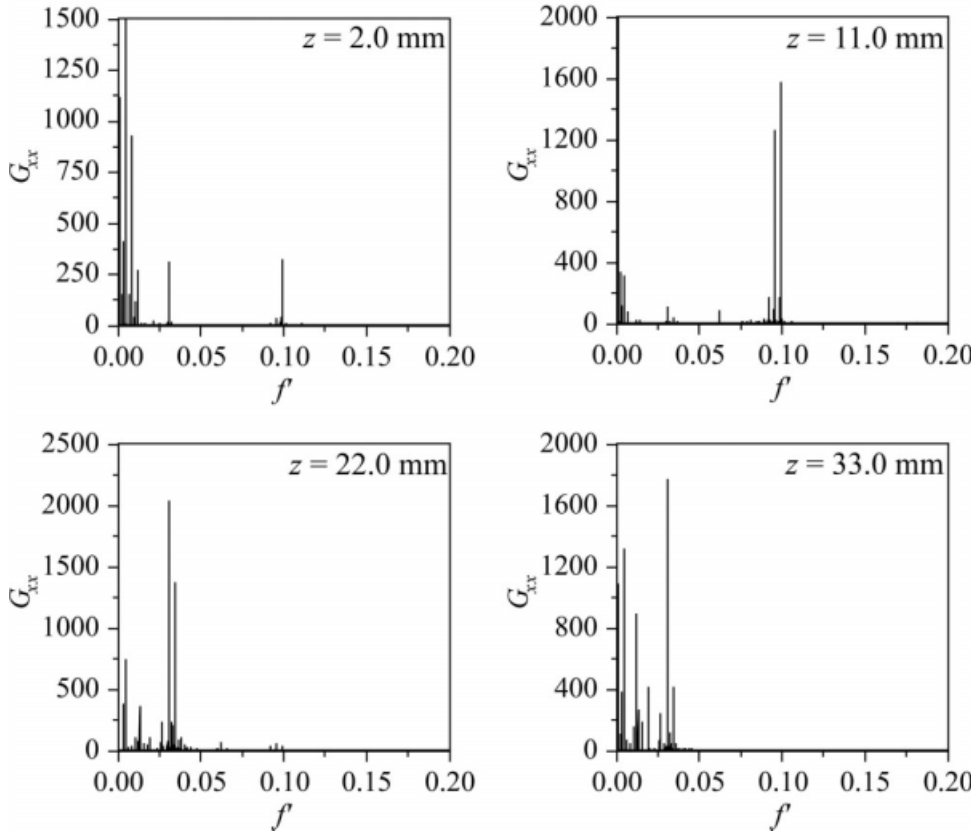

Figure 11. Power frequency spectra of v_x at *Re* = 300 throughout the mixing chamber axis.

$$\phi_{\text{vortex}} = \frac{2q_{\text{inj}}}{2V_{\text{vortex}}} = \frac{\upsilon_{\text{inj}} d}{A_{\text{vortex2D}}} = \frac{\upsilon_{\text{inj}} d}{\frac{\pi}{4}\left(D_{\text{vortex2D}}\right)^2} \tag{11}$$

where d and υ_{inj} are the injector width and superficial velocity at the injectors, respectively. A_{vortex2D} and D_{vortex2D} are the 2D vortex area and diameter. In terms of the Strouhal number Eq. 11 is expressed as

$$St = \phi \frac{d}{\upsilon_{\text{inj}}} = \frac{d^2}{\frac{\pi}{4}\left(D_{\text{vortex2D}}\right)^2} \tag{12}$$

Solving this equation for $St \approx 0.03$ gives $D_{\text{vortex2D}} \approx 10$ mm, and thus, downstream the chamber, the main feature of the flow is the passage of the *fully developed vortices* extending throughout the whole chamber width, as can be clearly seen from the flow maps shown in Figure 8.

2D/3D comparison

The flow features of 2D and 3D geometries have differences, such as:

- In 3D the jets form a pancake after impinging at a line defined by the injectors' axis, while in 2D the jets are bent towards the outlet and impinge at a point approximately 2.5 mm downstream the injectors' axis;
- A vortex street from the jets impingement point until the mixing chamber is seen in 2D simulations, whereas in 3D experiments the flow evolve to a parallel flow before the outlet;[21]
- The critical Reynolds number marking the onset of chaotic mixing mechanisms is 120 in the 3D mixing chamber[21] and 250 in the 2D case.[10]

Some of the differences in the power spectra from experimental data and CFD data are due to the different flow features or inherent to the experimental technique. A detailed analysis of the differences between experimental and CFD data power spectra is given in Santos et al.[7]

Nevertheless, in both 2D and 3D opposed jets mixers, the jets impingement point oscillation frequency was set from the same phenomenon: the formation of vortices downstream the jets. The CFD simulations facilitate the complete knowledge of flow variables in time and space, and so the CFD simulations were here used to confirm the mechanisms determining the jets oscillation frequency.

Conclusions

The comparison of the measured values of St with other values found in the literature is shown in Figure 12, from where it is clear the present contribution for a greater knowledge of the jets oscillation phenomenon. Most previous works had been done in the region closest to the transition Re from steady to chaotic flow regime, probably due to the difficulties reported by Johnson and Wood[9] of finding the typical frequency for higher values of Re.

From this work it is now clear that in confined opposed jets mixers the jets impingement point oscillates with frequencies around typical values. The oscillation frequency values are dictated by the geometry of the vortices occurring immediately downstream the jets impinging. If the vortices downstream the jets are not being formed, the two opposite streams do not engulf, and a clear segregation plan is formed throughout the mixing chamber axis.[10]

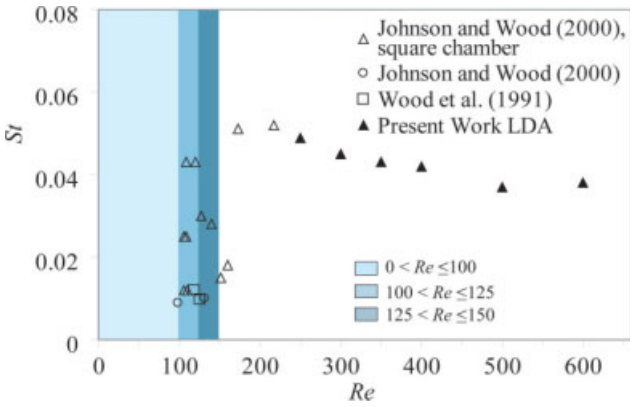

Figure 12. Variation of the Strouhal number with *Re* in several works found in literature.

[Color figure can be viewed in the online issue, which is available at www.interscience.wiley.com.]

The fact that the convective mixing mechanisms dictate the jets oscillations was the basis for a new patented concept: RIMCOP® (RIM with Control of Oscillation and Pulsation).[16,23] RIMCOP® machines are new generation RIM machines which allow Real Time control of mixing from vibration analysis schemes. The flow oscillations are measured outside the mixing chamber from dynamic monitoring of the static pressure at the opposed jets feeding pipes.[16] RIMCOP® is currently at the phase of industrial demonstration in LSRE/FEUP spin-off company: Fluidinova, Engenharia de Fluidos, SA. The Real Time control of mixing in RIM is a major breakthrough to the current state of the art in RIM, where the process is mainly verified from the molded parts characterization.

Acknowledgements

Financial support for this work was in part provided by national research grants FCT/POCTI/EQU/345115/2000, PTDC/CTM/72595/2006, and by LSRE financing by FEDER/POCI/2010, for which the authors are thankful. Ertugrul Erkoç acknowledges his Ph.D./scholarship by FCT (SFRH/BD/18901/2004). Ricardo J. Santos acknowledges financial support from POCI/N010/2006.

Notation

Roman symbols

A,B,a = constants of the viscosity formula for aqueous glycerol solutions.
d = injectors 3D diameter or 2D width.
d_1 = 3D prolate spheroid equatorial diameter.
d_2 = 3D prolate spheroid polar diameter.
D = mixing chamber 3D diameter or 2D width.
f = frequency.
f' = dimensionless frequency.
Fr = froude number.
g = gravity acceleration.
G_{xx} = spectral energy from slotted autocorrelation FFT.
G_{xy} = spectral energy from slotted crosscorrelation FFT.
n_s = number of samples in a velocity interval.
n_t = total number of samples.
N = total number of multiplications with non-empty slots.
q_{inj} = flow rate at each injector.
R_{xx} = discrete autocorrelation.

Re = reynolds number.
St = strouhal number.
t = time.
T = total time of a data series.
x,y,z = x, y, or z spatial coordinate.
X = mass fraction.

Greek letters

Δt = slot time span.
ϕ = typical frequency of oscillation.
μ = viscosity.
υ = velocity.
υ^* = dimensionless velocity.
ρ = density.
θ = temperature.
τ = fluid passage time in the mixing chamber.
ξ = time spent by a vortex translation between two points.

Subscripts

$_{\text{inj}}$ = at the injectors.
$_s$ = sampling or sample.
$_{x,z}$ = x or z spatial coordinate.

Literature Cited

1. Oertel G. *Polyurethane Handbook*. Munich: Hanser, 1985.
2. Malguarnera SC, Suh NP. Liquid injection molding I. An investigation of impingement mixing. *Polym Eng Sci*. 1977;77:111–115.
3. Coates PD, Johnson FA. Reaction injection processing of polymers. In: Monk JF, editor. *Thermosetting Plastics*. London: Addison Wesley Longman, 1997:238.
4. Teixeira AM. *Escoamento na Cabeça de Mistura de uma Máquina RIM (Flow in a RIM Machine Mixing Head)* [Ph.D.], Faculdade de Engenharia da Universidade do Porto; 2000.
5. Teixeira AM, Santos RJ, Costa MRPFN, Lopes JCB. Hydrodynamics of the mixing head in RIM: LDA flow-field characterisation. *AIChE J*. 2005;51:1608–1619.
6. Wood P, Hrymak AN, Yeo R, Johnson DA, Tyagi A. Experimental and computational studies of the fluid mechanics in an opposed jet mixing head. *Phys Fluids A*. 1991;3:1362–1368.
7. Santos RJ. Mixing mechanisms in reaction injection moulding—RIM. An LDA/PIV experimental study and CFD simulation [PhD], Faculdade de Engenharia da Universidade do Porto; 2003.
8. Santos RJ, Teixeira AM, Costa MRPFN, Lopes JCB. Operational and design study of RIM machines. *Int Polym Process*. 2002;17:387–394.
9. Johnson DA, Wood P. Self-sustained oscillations in opposed impinging jets in an enclosure. *Can J Chem Eng*. 2000;78:867–875.
10. Santos RJ, Teixeira AM, Lopes JCB. Study of mixing and chemical reaction in RIM. *Chem Eng Sci*. 2005;60:2381–2398.
11. Roy JC, Bertrand C, Palec GL. Numerical and experimental study of mixed and forced convection in a junction. *Int J Heat Mass Transfer*. 1994;37:1985–2006.
12. Devahastin S, Mujumdar AS. A numerical study of flow and mixing characteristics of laminar confined impinging streams. *Chem Eng J*. 2002;85:215–223.
13. Li X, Santos RJ, Lopes JCB. Modelling of self-induced oscillations in the mixing head of a RIM machine. *Can J Chem Eng*. 2007;85:45–54.
14. Johnson DA, Wood P, Hrymak AN. The effect of geometrical parameters on the flow field of an opposed jet RIM mix head: equal flow and matched fluids. *Can J Chem Eng*. 1996;74:40–48.
15. Erkoç E, Quadros PA, Santos RJ, Lopes JCB. Reaction injection moulding with oscillation and pulsation control technology–RIM-COP. Paper presented at: Rapid Product Development 2006, 2006; Marinha Grande, Portugal.
16. Erkoç E, Santos RJ, Nunes MI, Dias MM, Lopes JCB. Mixing dynamics control in RIM machines. *Chem Eng Sci*. 2007;62:5276–5281.
17. Kolodziej P, Macosko CW, Ranz WE. The influence of impingement mixing on striation thickness distribution and properties in fast polyurethane polymerisation. *Polym Eng Sci*. 1982;22:388–392.
18. Kolodziej P, Yang WP, Macosko CW, Wellinghoff ST. Impingement mixing and its effect on the microstructure of RIM polyurethanes. *J Polym Sci*. 1986;25:2359–2377.
19. Bell WA. Spectral analysis algorithms for the laser velocimetry: a comparative study. *AIAA J*. 1983;21:714–719.
20. Bell WA. Spectral analysis of laser velocimeter data with the slotted correlation method. Paper presented at:AIAA/ASME 4th Fluid Mechanics, Plasma Dynamics and Lasers Conference, 1986; Atalanta.
21. Santos RJ, Teixeira AM, Erkoç E, Dias MM, Lopes JCB. Hydrodynamics of the mixing chamber in RIM: PIV flow-field characterization. *AIChE J*. 2008;54:1153–1163.
22. Williamson CHK, Govardhan R. Vortex-induced vibrations. *Ann Rev Fluid Mech*. 2004;36:413–455.
23. Lopes JCB, Santos RJ, Teixeira AM, Costa MRPFN. Production process of plastic parts by reaction injection moulding, and related head device. US pat WO 2005/097477, 2005.
24. Waele S, Boersen PMT. Reliable LDA-Spectra by Resampling an ARMA-Modeling. *IEEE Trans Instrum Measure*. 1999;48:1117–1121.

Appendix

This appendix describes the data analysis procedures, namely the transformation of data from time domain into the frequency domain, f. This transformation is done through the Fast Fourier Transform, where the frequency power spectrum is usually represented by the FFT modulus, $|G(f)|$. In this work all the power spectra are normalized by their integral, i.e.

$$G(f) = \frac{|G(f)|}{\int |G(f)| df} \tag{13}$$

The FFT can only be used on *periodic time series*, i.e., where the time interval between points is fixed. LDA data was obtained in *time stamp* mode where each particle generates a velocity datum that is stored with the time information, and thus the time series from LDA measurements is *non-periodic*. Computational Fluid Dynamics, CFD, simulations were performed with an adaptive time step,[4] and thus the time series from the simulated flow field, is also *non-periodic*.

There are several techniques to generate series suitable for the FFT from *non-periodic* time series. The most common are the *slotting techniques* such as the slotted correlation method,[19,20] and the *re-sampling techniques*.[24] The slotted correlation is equivalent to the autocorrelation function, but modified for *non-periodic* time series, and it gives a measure of how repetitive the signal is by correlating intervals along the whole series.

In the slotted correlation, each point, $\upsilon_x(t_i)$, is multiplied by the average of a time slot, $\overline{\upsilon_x(t_j)}$, centered at $t_i + kt_s$ with a slot width Δt. For a given kt_s the slotted correlation value is given by

$$R_{xx}(kt_s) = \frac{1}{N}\sum_{i=1}^{N} \upsilon_x(t_i)\overline{\upsilon_x(t_j)},\ t_j \in \left[t_i + kt_s - \frac{\Delta t}{2}, t_i + kt_s + \frac{\Delta t}{2}\right], \quad k = 1, 2, \ldots, n \tag{14}$$

For each kt_s, the total number of multiplications with non-empty slots is N. The slotted correlation has two parameters:

- The *spacing* of the time series, t_s. According to the Nyquist criterion the maximum detectable frequency from a time series is

$$f_{max} = \frac{f_s}{2} \tag{15}$$

where f_s is the acquisition data rate of the time series. The chosen t_s should then be close to $1/f_s$, in order not to overcome the Nyquist criteria since $f_{max} = 1/2t_s$.

- The slot width, Δt. If the chosen Δt is too high, the power spectrum can be smoothed and the energy peaks at higher frequencies dumped. If the slot width is too narrow, it may happen that most of the slots become empty.

The first step of the data analysis procedure is the computation of the slotted autocorrelation, R_{xx}, then the FFT of the R_{xx} is computed. The power spectrum, G_{xx}, is obtained from the normalized modulus of the FFT. The details of the used software and numeric routines for the data analysis are presented in Santos.[7]

Manuscript received Feb. 19, 2008, revision received Sept. 2, 2008, and final revision received Nov. 21, 2008.